Materials Advances

ROYAL SOCIETY OF CHEMISTRY

PAPER

View Article Online
View Journal | View Issue

Cite this: *Mater. Adv.*, 2023, 4, 4798

Growth factor-encapsulated triphasic scaffolds of electrospun polylactic acid–polycaprolactone (PLA–PCL) nanofibrous mats combined with a directionally freeze-dried chitosan hydrogel for periodontal tissue regeneration

Weihan Hua,[a] Jie Xiang,[a] Yeke Wu,[b] Wei Yang *[c] and Lixing Zhao *[a]

Cementum, periodontal ligament, alveolar bone, and gingiva make up the three-dimensional, multicellular structure known as periodontal tissue, which is crucial for maintaining the healthy alignment and function of teeth. Simulating the highly layered and orderly structure of periodontal tissue is the key to achieving its regeneration. In this study, through electrospinning, directional freeze-drying, and cross-linking, we successfully fabricated poly lactic acid (PLA)–poly ε-caprolactone (PCL) electrospun nanofibrous mats with the freeze-dried chitosan of the directionally arranged microporous channel structure. Moreover, we used nanoparticles to load three different growth factors of the target layer. We constructed triphasic scaffolds that simulated the physiological periodontal tissue. These scaffolds with superior mechanical properties were tested *in vitro* with periodontal ligament stem cells (PDLSCs), and the results supported that the triphasic scaffolds with growth factors had superior biocompatibility and reduced cytotoxicity. Furthermore, we performed *in vivo* experiments, and the triphasic scaffolds loaded with growth factors were able to promote the repair of periodontal defects by promoting the formation of alveolar bone-like tissue, periodontal ligament-like tissue, and cementum-like tissue. The successful construction of the triphasic scaffold provides a novel approach for remodeling the physiologic organization and function of the periodontal tissue with multiphasic scaffolds.

Received 26th July 2023,
Accepted 7th September 2023

DOI: 10.1039/d3ma00465a

rsc.li/materials-advances

Introduction

During the process of dental and maxillofacial development, the microenvironment of dental follicles promotes stem cells to differentiate into cementoblasts, fibroblasts, and osteoblasts, thereby forming the cementum, periodontal ligament, and alveolar bone. However, this microenvironment no longer exists after the completion of periodontal tissue, resulting in great difficulties in self-repair.[1–4] Moreover, the chronic infectious disease periodontitis might occur with bacterial infection or trauma, which leads to the destruction of periodontal tissues and even tooth loss, and seriously affects the oral health-related quality of life.[5–7] At present, the purpose of inflammation control is mainly achieved by removing plaque and local irritants,[8,9] while for the structural-functional reconstruction of defects, there has been no efficient therapeutic strategy that can only prevent further tissue destruction yet.[10]

With the development of biomaterials, tissue engineering technology has been continuously shown to be a promising approach for periodontal tissue regeneration. At present, most scaffolds for periodontal tissue engineering are biphasic constructs, which focus mainly on the ectopic or *in situ* regeneration of periodontal ligaments and the restoration of alveolar bone height. The creation of new periodontal ligament-like tissue and alveolar bone-like tissue is visible in the defect location after ectopic or *in situ* implantation of these scaffolds *in vivo*.[11–16] In our previous study, we synthesized a 3D multilayered electrospun scaffold to simulate the microenvironment of periodontium.[17] It was observed that aligned electrospun nanofibers could induce cells in an oriented alignment through contact guidance and cell–fiber interactions, which further promoted cytoskeleton rearrangement to guide oriented tissue regeneration. Notably, the periodontal complex has a stratified sandwich-like structure, with periodontal ligament located in

[a] *State Key Laboratory of Oral Diseases & National Clinical Research Center for Oral Diseases & Department of Orthodontics, West China Hospital of Stomatology, Sichuan University, China. E-mail: zhaolixing@scu.edu.cn*
[b] *Department of Stomatology, Hospital of Chengdu University of Traditional Chinese Medicine, Chengdu, China*
[c] *College of Polymer Science and Engineering, Sichuan University, State Key Laboratory of Polymer Materials Engineering, Chengdu 610065, Sichuan, China. E-mail: weiyang@scu.edu.cn*

the middle layer, containing directionally arranged collagen fiber bundles inserted into the mineralized cementum and alveolar bone at both ends. Thus, the three components are connected as a whole.[11–16] Periodontal tissue engineering can only fully simulate the physical structure and function of the physiological periodontal tissue by achieving cementum regeneration and forming an anchoring connection structure-the Sharpey fiber, at the interface between cementum, periodontal ligament, and alveolar bone.[18–21]

According to recent research, the incorporation of poly lactic acid (PLA) into poly ε-caprolactone (PCL) can compensate for the shortcomings of the two and make the performance of the material better.[22,23]Electrospun PLA–PCL nanofibrous scaffolds would have a shorter degradation time, higher mechanical properties (*e.g.*, stiffness and modulus), and better bioactivity than pure PCL scaffolds. Besides, researchers have found that PLA–PCL (wt/wt, 70/30) showed that the separation of the phase would not be a major concern.[24,25] In this study, we have successfully developed PLA–PCL (wt/wt, 70/30) nanofibrous mats using an electrospinning technique and chitosan with an orderly aligned microporous channel structure by directional freeze-drying technology.

Besides, bone morphogenetic protein 2 (BMP2), recombinant human cementum protein 1 (rhCEMP1), and connective tissue growth factor (CTGF) are encapsulated into the target layer of the scaffold by chitosan-stabilized bovine serum albumin (BSA) nanoparticles. After that, the shape, structure, surface hydrophilicity, drug loading, and release of the nanoparticle were examined. And the *in vitro* micromorphology, mechanical properties, biocompatibility, and cytotoxicity of the triphasic scaffolds were also determined. Additionally, tissue regeneration was evaluated after the nanofibrous composite was implanted into rat periodontal defects. Collectively, our studies looked at the potential of a biomimetic multiphasic scaffold in the field of periodontal tissue regeneration, potentially providing light on complex tissue regeneration with clinical viability.

Materials and methods

Scaffold preparation

Materials. Bovine serum albumin (BSA) was purchased from BioFroxx (Einhausen, Hesse, Germany), high viscosity chitosan (CHI) was purchased from Shanghai Ruiyong biological Co., Ltd (Shanghai, China), polylactic acid (PLA), and polycaprolactone (PCL) were purchased from Corbion Purac (Amsterdam, Netherlands) and Perstorp Chemical (Shenzhen, China), and other chemical reagents were purchased from Kelong Chemical Reagents (Chengdu, China). Bone morphogenetic protein 2 (BMP2) was purchased from MedChemExpress (Monmouth junction, NJ, USA), recombinant human cementum protein 1 (rhCEMP1) was purchased from Cloud-Clone Corp (Katy, TX, USA), and connective tissue growth factor (CTGF) was purchased from PeproTech (Rocky Hill, NJ, USA).

Nanoparticles preparation. Nanoparticles with growth factor slow-release function (hereinafter referred to as ''nanoparticles (NPs)'') are prepared by the modified desolation technique reported in previous literature.[26] In a nutshell, BSA (100 mg) was dissolved in deionized water (10 mL), growth factors (100 μL containing 100 μg of BMP2, rhCEMP1, or CTGF) were added, and the mixture was magnetically stirred for ten minutes. Next, ethanol (40 mL) was pumped into the 1% BSA solution using a micro syringe pump at a rate of 2 mL min^{-1}, and the mixture was continuously stirred overnight. Then it was pumped with 40 mL of CHI solution (1 mg mL^{-1}, dissolved in 1% acetic acid solution), which was added at a rate of 0.5 mL min^{-1}. After the mixture was centrifuged at 12 000 rpm for 20 minutes white precipitated aggregates were collected and stored at −20 °C. The supernatant was collected for further research on encapsulation effectiveness and *in vitro* release of GFs. Finally, the precipitate was freeze-dried for 48 h in a vacuum freeze dryer (Beijing Boyikang Experimental Instrument Co., Ltd, Beijing, China) to obtain NPs loaded with BMP2, rhCEMP1, and CTGF (NPs-BMP2, NPs-rhCEMP1, and NPs-CTGF).

Electrospinning of PLA–PCL. The NPs (NPs-BMP2 and NPs-rhCEMP1) of 100 μg were ultrasonically redispersed in 2.5 mL of dimethylformamide (DMF). A PLA–PCL (wt/wt, 70/30) blend was dissolved in 7.5 mL dichloromethane (DCM) to form a 12 wt% electrospinning solution. The electrospun solution was mixed under continual stirring overnight. With an applied voltage of 12 kV, the electrospun process was carried out at a tip-to-collector distance of 17 cm with a feeding rate of 3 mL h^{-1} and a collection rate of 100 rpm. All these nanofiber scaffolds were gathered, vacuum-dried for 48 hours at ambient temperature to get rid of any remaining solvents, and then kept at −20 °C. The pure PLA–PCL electrospun nanofibers were created, which served as a control group, without the GFs.

Fabrication of nano-biomimetic scaffold. The fabrication scheme of triphasic scaffolds loaded with different growth factors is shown in Fig. 1(A). 2 wt% CHI was dissolved in 1% acetic acid solution by stirring for 2–3 h at 50 °C. Then, we added Genipin as a crosslinker into the CHI solution at 0.5% w/w. The alveolar-bone compartment (PLA–PCL-NPs-BMP2) composed of four layers of electrospun nanofibers was stacked on the bottom of the Petri dish, and the layers were compacted with hybrid CHI-genipin hydrogels. Thereafter, the periodontal-ligament compartment (CHI-NPs-CTGF) comprised of 100 μg of NPs-CTGF and the CHI solution stated before were uniformly mixed but not yet cross-linked and added into the Petri dish to achieve the liquid level of approximately 1 mm, and the reaction mixture was cross-linked in a fume hood for 24 h. Meanwhile, the cementum compartment (PLA–PCL-NPs-rhCEMP1) consisted of two layers of electrospun nanofibers stacked on the bottom of another dish and compressed with CHI–genipin mixture followed by 24 h of cross-linking. After there was no fluidity in CHI-NPs-CTGF, the cementum compartment was superimposed on top of the periodontal-ligament compartment, and the cross-linking was continued for 24 h to integrate the three components into a whole composite. Afterward, directional lyophilization[27] was carried out. Finally, the scaffolds were sectioned into square blocks of 3 × 2 × 1 mm^3 (Fig. 1(B)).

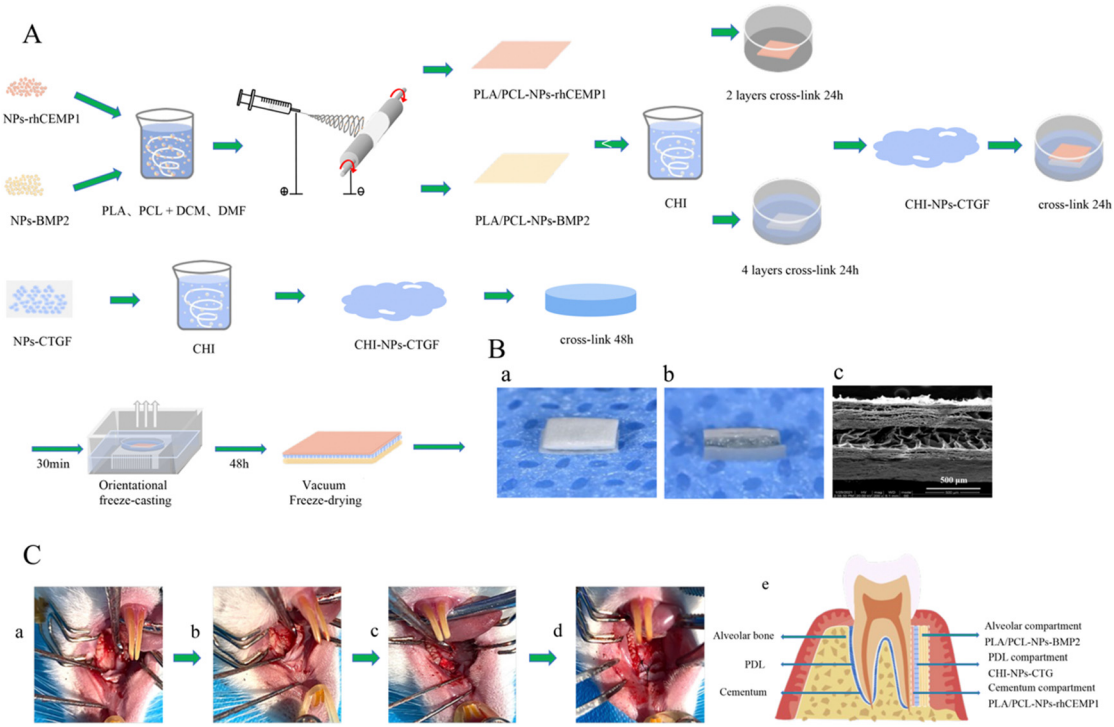

Fig. 1 Fabrication of triphasic scaffolds. (A) Schematic diagram of the preparation process of triphasic scaffolds and growth factors. (B) Morphology of the triphasic scaffolds. (a) and (b) Macroscopic morphology of the triphasic scaffolds. (c) SEM image of the cross-section of triphasic scaffolds. (C) Construction of rat periodontal tissue defects. (a)–(d) Defect establishment and scaffold implantation procedure. (e) Schematic diagram of scaffold implantation in the defect, the white dotted area showed the defect and where to implant the scaffold.

Scaffold characterization

SEM observation. TM F50 scanning electron microscopy (SEM) (FEI, Eindhoven, Netherland) was used to observe the morphology of NPs, as well as the incorporation of them in the electrospun nanofiber mats and CHI hydrogel. The particle size distribution was then calculated using the dynamic light scattering (DLS) method with BI-200SM after the NPs had been distributed in 100% ethanol (Brookhaven, MS, USA). Finally, the average diameter of electrospun nanofibers (PLA–PCL-NPs-BMP2 and PLA–PCL-NPs-rhCEMP1) and the pore size of CHI hydrogel (CHI-NPs-CTGF) were evaluated by random measurement at 100 different points in the SEM images using Image J software (National Institutes of Health, Bethesda, MD, USA).

Hydrophilicity properties. Using a dynamic water contact angle (WCA) measuring device (Kruess Scientific Instruments, Germany), the wettability of the electrospun nanofibers was assessed to determine the impact of NP loading on the hydrophilicity of triphasic scaffolds. The pure PLA–PCL electrospun nanofiber was employed as the control and three drops of water were put onto each sample in various locations. The contact angle between the water and membrane surface was then recorded after 20 seconds. Three parallel samples were set for each group of materials.

Growth factors release. The supernatant mentioned above was used to assess the GFs encapsulation efficiency (EE) (EE% = $c_1/c_2 \times 100\%$, where c_1 stands for the concentration of growth factors contained in the NPs and c_2 stands for the overall concentration of growth factors in the formulation).

Besides, 13 μg PLA–PCL-NPs-BMP2 (containing 1 ng BMP2), 65 μg PLA–PCL-NPs-rhCEMP1 (containing 5 ng rhCEMP1), and 110 μg CHI-NPs-CTGF (containing 10 ng CTGF) were shaken and incubated with 0.5 mL phosphate buffer saline (PBS) at 37 °C. On the certain time-points of 6 h, 12 h, 1 d, 3 d, 5 d, 7 d, 9 d, 12 d, 15 d, 18 d, 21 d, 25 d, and 30 d, 0.5 mL of the PBS solution was removed and BMP2, rhCEMP1, and CTGF concentrations were measured using a BMP2 enzyme-linked immunosorbent assay (ELISA) kit (LinkBio, Wuhan, China), rhCEMP1 ELISA kit (Huamibi, Wuhan, China), and CTGF ELISA kit (LinkBio, Wuhan, China). The withdrawn solution was replaced with the same volume of brand-new PBS. Software called CurveExpert was used to establish the standard curve (Huami Bio, Wuhan, China). Three parallel samples were set for each group of materials.

Mechanical properties. Tensile tests were conducted on the triphasic scaffolds at room temperature using a universal material testing system (Instron, model 5567, Boston, MA, USA). The software was running at a pace of 2 mm min^{-1} until the scaffold was pulled apart, and the samples were sliced into rectangles measuring 30 mm by 5 mm. Three parallel samples were set for each group of materials.

In vitro evaluations

Human PDL stem cells (hPDLSCs). Premolars (12–18 years old) were obtained by premolar extractions for orthodontic purposes. Each tooth was washed briefly before the PDL tissues were cut away from the middle third of the root surface. PDL tissues were

chopped into minute bits of 1 mm^3. The tissues were then digested for 20 minutes at 37 °C using 3 mg mL^{-1} type I collagenase and 4 mg mL^{-1} dispase (both from Sigma-Aldrich, St. Louis, MO, USA). Using the limited dilution approach, single-cell-derived colony cultures were created to produce homogeneous populations of human PDL stem cells (hPDLSCs). The complete medium used was DMEM medium with 10% fetal bovine serum and 1% penicillium–streptomycin. hPDLSCs at passages 3rd–5th were used in the following study.

The isolated hPDLSCs were observed under a U-LH100L-3 inverted phase contrast microscope (Olympus, Tokyo, Japan). For identification of the mesenchymal stem cells phenotype, hPDLSCs (5×10^5 cells) were incubated with allophycocyanin (APC)-, propidium iodide (PI)- or fluorescein isothiocyanate (FITC)-conjugated monoclonal antibodies for human CD90, CD146, and CD45 (BD Biosciences, Franklin Lakes, NJ, USA), or isotype-matched control IgGs. Then, a Beckman Cytomic FC500 flow cytometer (Beckman Coulter, Brea, CA, USA) was used to analyze the flow cytometry. Three parallel samples were set for each group of materials at each time point.

Cell culture. The scaffolds which were sterilized for 4 hours by ultraviolet light were divided into sections of 2.1 cm diameters and put into a 12-well culture plate. Then they were immersed in PBS with 10% penicillin–streptomycin for 30 min and washed with PBS three times (5 min per time), followed by pre-inoculation with DMEM medium without serum or antibodies at 37 °C overnight. 2.5×10^4 hPDLSCs were planted in each well on the surface of the scaffolds. All cells were grown in an incubator at 37 °C and 5% CO_2, with medium changes occurring every 2–3 days.

SEM observation. On the third and seventh days after the hPDLSCs were inoculated, all samples were fixed with 4% paraformaldehyde and freeze-dried for 48 h. After gradient ethanol dehydration, a SEM was used to observe the cell morphology on the surfaces of PLA/PCL-NPs-BMP2, PLA/PCL-NPs-rhCEMP1, and PLA/PCL which was used as a control.

Live/dead staining. The live/dead cell double staining kit (US Everbright Inc., Suzhou, China) was used to confirm the cytotoxicity of the scaffolds. After 1, 4, 7, and 10 days of inoculation, all samples were stained for 20 minutes at 37 °C in the dark with calcein-AM and PI. A confocal laser scanning microscope (CLSM) was then used to capture images of the cells (Olympus FV3000, Olympus, Tokyo, Japan). The experimental groups include triphasic scaffolds with growth factors, triphasic scaffolds without growth factors, porous CHI control, and blank control. Three parallel samples were set for each group of materials at each time point.

Cell proliferation assay. Cell proliferation was measured using the CCK-8 technique. After 1, 4, 7, and 10 days of inoculation, 10% CCK-8 (MedChem Express, NJ, USA) was added and cells were incubated at 37 °C for 2 hours. A Varioska LUX microplate reader (Thermo Fisher Scientific, Waltham, MA, USA) was used to detect the samples' absorbance at 450 nm. The experimental groups include triphasic scaffold with growth factors, triphasic scaffold without growth factors, porous CHI control, and blank control. Three parallel replicates were set for each group at each time point. Three parallel samples were set for each group of materials at each time point.

Real-time quantitative polymerase chain reaction (qPCR) analysis. Real-time quantitative reverse transcription polymerase chain reaction (RT-qPCR) was carried out to evaluate the gene expression levels of the *Runx2*, *alkaline phosphatase (ALP)*, *cementum attachment protein* (*CAP*), *cementum protein 1* (*CEMP1*), *Periostin*, *Scleraxis*, *collagen*, *type I*, *alpha 1 (COL1A1)*, and *collagen*, *type III*, and *alpha 1 (COL3A1)*. The experimental groups were set as PLA–PCL-NPs-BMP2, PLA–PCL-NPs-rhCEMP1, CHI-NPs-CTGF, PLA–PCL, CHI, and blank control group. After culture in the complete DMEM medium with osteogenic induction supplements (25 μM mL^{-1} β-phosphoglyceride, 0.05 μg mL^{-1} ascorbic acid, and 0.01 nM mL^{-1} dexamethasone) for 7 days, total RNA was extracted using a TRIzol reagent (Invitrogen, Karlsruhe, Germany), and cDNA was obtained using the TaKaRa PrimeScript Reverse Transcription Kit (TaKaRa, Kyoto, Japan). Sangon Biotech Co., Ltd (Shanghai, China) provided the primers utilized in the procedure, and the primer sequences are displayed in Table 1. The internal control was the common gene glyceraldehyde 3-phosphate dehydrogenase (GAPDH). Three parallel samples were set for each group of materials at each time point.

In vivo studies

Surgical procedures. The Sichuan University Ethics Committees (WCHSIRB-D-2020-288) authorized all experimental protocols, and all studies were carried out in accordance with the ARRIVE and the NIH Guide. Twenty-five Sprague-Dawley (SD) rats (female, 8 weeks old, 250 ± 25 g) were randomly divided into four groups ($n = 5$ for each group): triphasic scaffold with growth factors, triphasic scaffold without growth factors, monophasic scaffold (CHI), and monophasic scaffold (PLA–PCL) (Table 2).

Table 1 Primers used for real-time quantitative reverse transcription polymerase chain reaction (qRT-PCR) analysis

Gene	Forward (5′-3′)	Reverse (5′-3′)
RUNX2	CCGCCTCAGTGATTTAGGGC	GGGTCTGTAATCTGACTCTGTCC
ALP	AACATCAGGGACATTGACGTG	GTATCTCGGTTTGAAGCTCTTCC
CAP	TCCAGACATTTGCCTTGCTT	TTACAGCAATAGAAAAACAGCATGA
CEMP1	GGGCACATCAAGCACTGACAG	CCCTTAGGAAGTGGCTGTCCAG
Periostin	CTCATAGTCGTATCAGGGGTCG	ACACAGTCGTTTTCTGTCCAC
Scleraxis	AGAAAGTTGAGCAAGGACC	CTGTCTGTACGTCCGTCT
COL1A1	GTGCGATGACGTGATCTGTGA	CGGTGGTTTCTTGGTCGGT
COL3A1	TTGAAGGAGGATGTTCCCATCT	ACAGACACATATTTGGCATGGTT
GAPDH	GGAGCGAGATCCCTCCAAAAT	GGCTGTTGTCATACTTCTCATGG

Table 2 Vitro experiment. Among them, the triphasic scaffold group with different growth factors and the triphasic scaffold group without growth factors were described above. The monophasic chitosan group was CHI-NPs-CTGF lyophilized stent, and the monophasic electrospinning scaffold was 4 layers PLA/PCL-NPs-BMP2 and 2 layers PLA/PCL-NPs-rhCEMP1 electrospinning nanofibers together

	Triphasic	GFs	Directional lyophilization
Triphasic scaffold (with GFs)	+	+	+
Triphasic scaffold (without GFs)	+	–	+
Monophasic scaffold (CHI-NPs-CTGF)	–	+	+
Monophasic scaffold (PLA/PCL)	–	+	–

After intraperitoneal anesthesia by 1% pentobarbital sodium (50 mg kg^{-1}), the upper and lower jaws of the rats were separately fixed to expose the operative area. 2% lidocaine was injected into the surgical site to reduce discomfort. We had a vertical full-thickness incision on the left maxillary first molars' proximal palatal side. Using spherical burs and generous saline irrigation, the cementum covering the roots, PDL, and alveolar bone were removed. Then, a rectangular periodontal defect of typical dimensions of 3 mm × 2 mm × 1 mm was made. Afterward, the disinfected scaffolds were implanted into the defect (Fig. 1(C)). The rats were put down with an overdose of 40% sodium pentobarbital 12 weeks following the operation. The maxilla samples were collected, fixed for 48 hours in 4% paraformaldehyde, and then preserved in 70% ethanol.

Micro-CT analysis. Scans were performed by a SCANCO MEDICAL μCT50 Micro-CT (SCANCO Medical AG, Zurich, Switzerland) at a source voltage of 70 kV, source current of 140 μA, and voxel resolution of 18 μm. The micro-CT analysis program used the scans to create 3D models of the flaws. The region of interest (ROI), which covered the range of about 2 mm on the root surface in the buccal-lingual direction and the range from tooth cervix to root apex in the occlusal-gingival direction, was drawn from the first slice containing the defect and moved distally until the defect area disappeared. The quantitative analysis of the bone volume fraction (bone volume/total volume, BV/TV) was performed on the scanned image to assess the extent of periodontal bone regeneration in the defect area following scaffold implantation.

Histological analysis. After micro-CT scanning, the maxilla samples were decalcified in 10% EDTA solution for 8 weeks. H&E, Masson (Solarbio) staining, and immunohistochemical staining of BMP-2 (Abcam) were performed. The Nikon ECLIPSE 80i microscope (Nikon, Tokyo, Japan) was used to scan the stained slides. On three randomly chosen H&E-stained sections of each group, the angle between the long axis of the fibers and the new cementum was analyzed using Image J software.

Statistical analysis

The data were analyzed using the Statistical Package for Social Science (version 25.0; SPSS, Chicago, IL, USA) for Windows. Data were expressed as mean ± SD, and each experiment was repeated at least three times. The one-way analysis of variance (ANOVA) with Tukey's *post hoc* test was used to statistically compare the groups. Statistics were considered significant when $*P < 0.05$.

Results

Micromorphology of NPs, electrospun nanofiber mats, and CHI hydrogels

The micromorphology of the CHI-stabilized BSA NPs was observed by SEM and is shown in Fig. 2(A). The results measured by DLS showed that the three NPs were similar in diameter: 434.72 nm (NPs-BMP2), 441.70 nm (NPs-rhCEMP1), and 425.64 nm (NPs-CTGF), with an average diameter of 434.02 ± 8.05 nm.

In contrast to the pure PLA–PCL nanofibers, which showed a smooth appearance, both the PLA–PCL-NPs-BMP2 and the PLA–PCL-NPs-rhCEMP1 nanofibers presented a slightly rougher surface with small nodules bulging outward, demonstrating the successful incorporation of NPs-BMP2 and NPs-rhCEMP1 within the nanofiber matrix during the electrospinning process (Fig. 2(B)). The average diameters of each nanofiber were approximately 359.85 ± 91.60 nm (PLA–PCL-NPs-BMP2), 350.41 ± 8 6.00 nm (PLA–PCL-NPs-rhCEMP1), and 370.96 ± 127.02 nm (PLA–PCL), without statistically significant differences among them ($P > 0.05$), indicating that the loading of NPs-BMP2 and NPs-rhCEMP1 had no remarkable influence on the diameter of the electrospun nanofibers. For pore size distributions, the average pore size of CHI-NPs-CTGF was 123.48 ± 43.17 μm, whereas the pore size of pure CHI (162.90 ± 46.78 μm) was much larger ($P < 0.05$) (Fig. 2(C)). Importantly, all these diameters and pore sizes are within the nanometer range and close to the natural ECM fibers, which represents favorable biomimicry.[28]

Characterizations of scaffolds

The hydrophilicity of the electrospun nanofibers. Fig. 3(A) shows the results of the hydrophilic test. The contact angles obtained for PLA–PCL-NPs-BMP2, PLA–PCL-NPs-rhCEMP1 and pure PLA–PCL electrospun nanofibers were 126.25 ± 3.42°, 127.25 ± 3.01°, and 138.85 ± 4.43°, respectively. All the values were greater than 90°, indicating that the materials remained at a certain degree of hydrophobicity. However, the contact angles of PLA–PCL-NPs-BMP2 and PLA–PCL-NPs-rhCEMP1 were significantly lower than that of the pure PLA–PCL control ($P < 0.05$). These findings imply that adding NPs enhanced the wettability of electrospun nanofibers, which can be attributed to modifications made to the hydrophilic hydroxyl and amino groups expressed on the NPs as well as to modifications made to the composite fiber's surface roughness.[29]

***In vitro* release study of the GFs.** Firstly, the EE measurement of NPs by ELISA were 92.95 ± 1.31% (NPs-BMP2), 91.07 ± 1.88% (NPs-rhCEMP1), and 89.95 ± 0.78% (NPs-CTGF), with an average of 91.32 ± 1.52% (Fig. 3(B)). Then, *in vitro* release of the GFs loaded in NPs showed that they were in a stable release state until the 30th day, and the cumulative release rates were 77.53% (BMP2), 75.31% (rhCEMP1), and 78.20% (CTGF). The release of GFs occurred in two stages: early burst release and

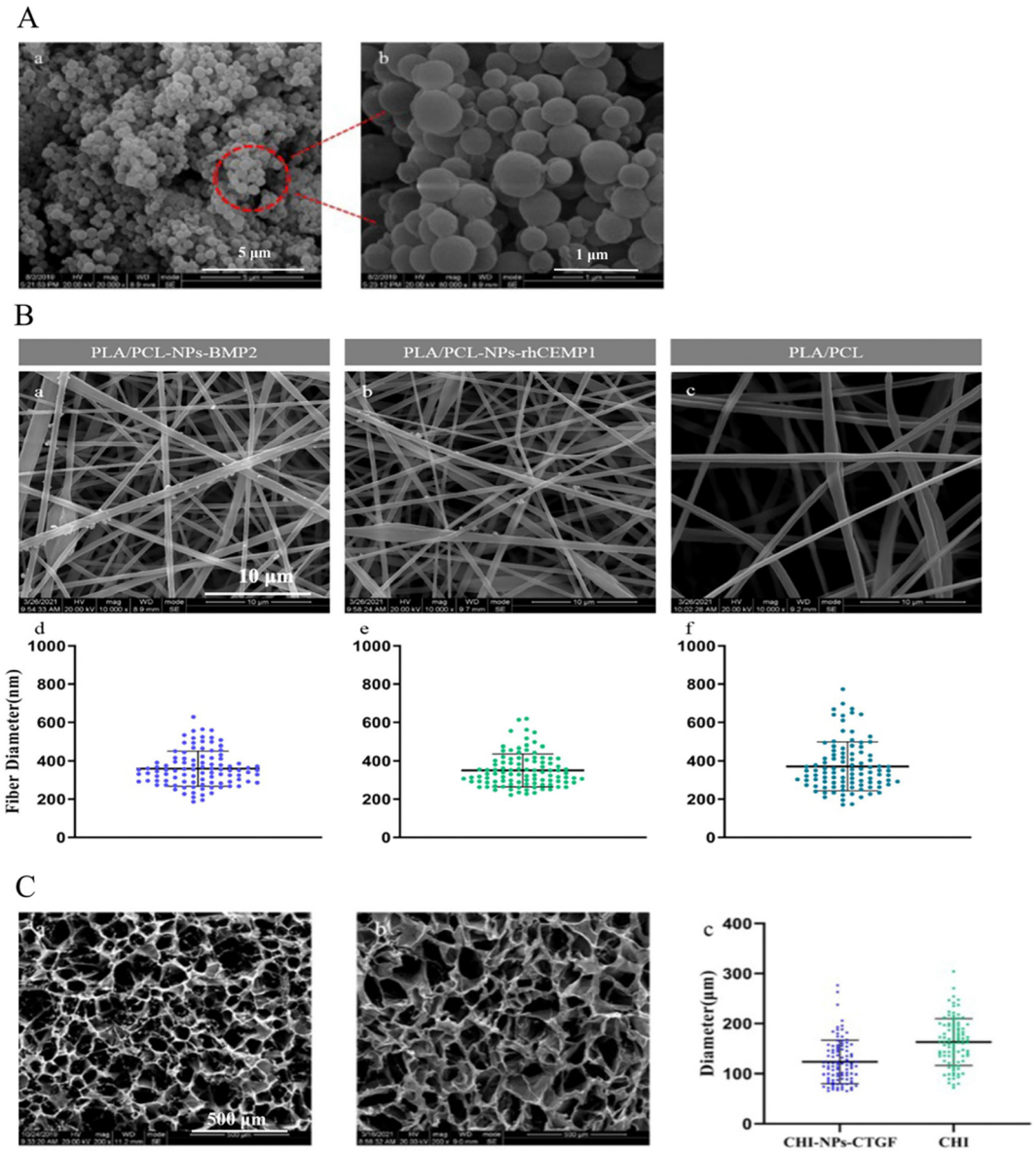

Fig. 2 (A) SEM images of nanoparticles loaded with growth factors (a: 5 μm; b: 1 μm). (B) Microstructure of electrospun nanofibers loaded with nanoparticles. (a) SEM image of PLA/PCL-NPs-BMP2 electrospun nanofibers. (b) SEM image of PLA/PCL-NPs-rhCEMP1 electrospun nanofibers. (c) SEM image of pure PLA/PCL electrospun nanofibers. (d)–(f) Scatter diagrams of nanofiber diameter distribution of PLA/PCL-NPs-BMP2, PLA/PCL-NPs-rhCEMP1, and pure PLA/PCL electrospun nanofibers. (C) Microscopic morphology of chitosan freeze-dried scaffold loaded with nanoparticles. (a) SEM image of CHI-NPs-CTGF scaffold. (b) SEM image of pure CHI scaffold. (c) Scatter diagram of the pore size distribution of CHI-NPs-CTGF and pure CHI scaffolds.

late sustained release.[30] Approximately 61.26% of CTGF were released during the first three days, followed by smaller increases in the release thereafter. More intriguingly, the release profiles of the three GF-loaded systems within the triphasic scaffolds revealed a sequential release pattern, in which the majority of CTGF and BMP2 were released during the first five days, while rhCEMP1 was initially released relatively slowly before showing a slight acceleration but constant release.

Micromorphology of the triphasic scaffolds. Then, the general structure and macro-morphology of the fabricated triphasic scaffolds loaded with various GFs are shown in Fig. 1(B), which could be visibly divided into three distinct components with the PDL compartment (turquoise porous CHI layer) in the middle and the cementum, and alveolar compartments (ivory-white stacking electrospun nanofibrous layer) at both ends. SEM images further revealed that the highly homogenous CHI channels were closely interconnected with the electrospun nanofibers at a certain angle to enable the structural integrity to be maintained and distinct interfaces were formed among the three layers. Afterward, the alveolar bone layer ranked first with approximately 310.58 ± 32.08 μm in thickness, and the PDL layer took second place with a thickness of 250.46 ± 22.43 μm, whereas the cementum layer was the thinnest of about 108.48 ± 7.99 μm.

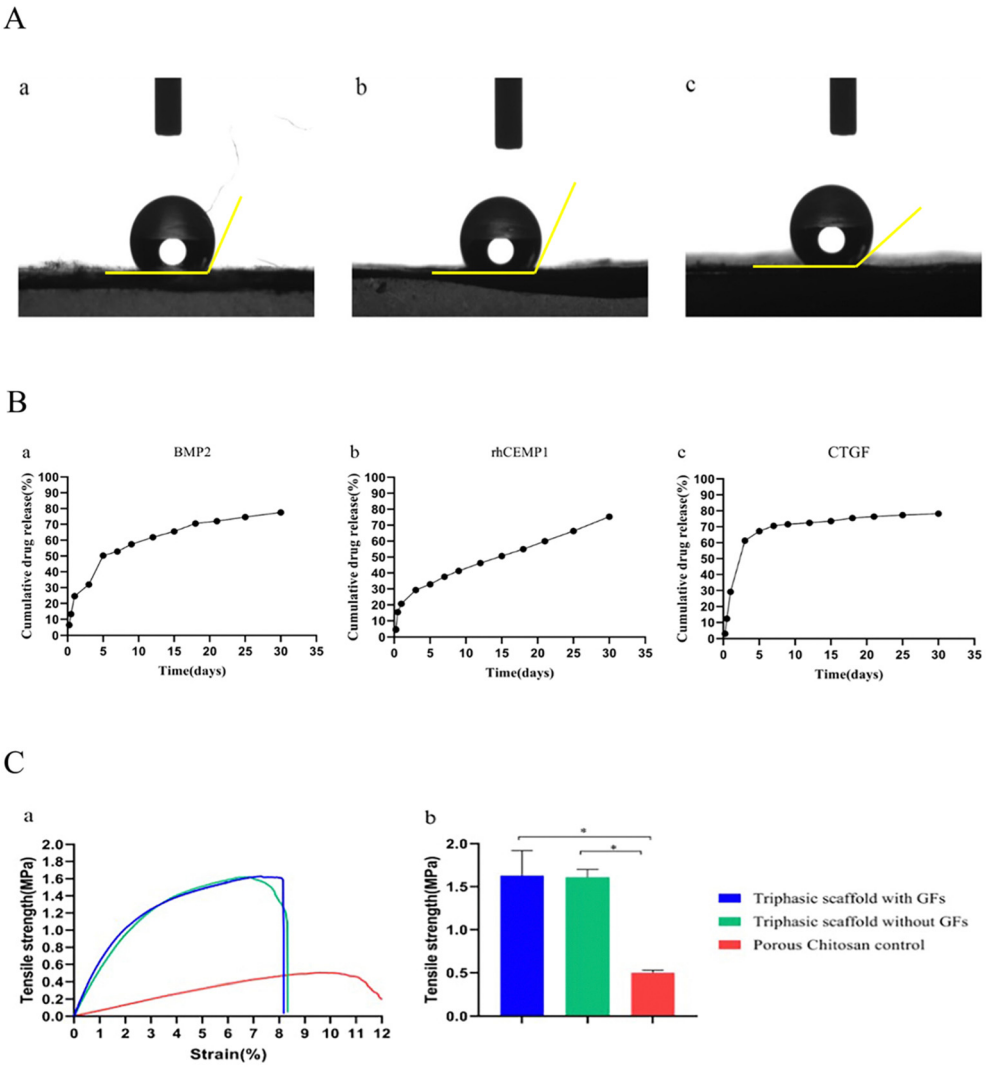

Fig. 3 (A) Hydrophilic surface of the electrospun nanofibers. (a) PLA/PCL-NPs-BMP2 electrospun membrane. 126.25 ± 3.42°. (b) PLA/PCL-NPs-rhCEMP1 electrospun membrane. 127.25 ± 3.01°. (c) pure PLA–PCL electrospun membrane. 138.85 ± 4.43°. (B) Growth factors sustained–release curves. (a) BMP2. (b) rhCEMP1. (c) CTGF. (C) Comparison of the tensile properties of scaffolds. (a) Tensile stress–strain curves of different scaffolds. (b) Comparison of maximum tensile strengths of different scaffolds. Triphasic scaffold with GFs, triphasic scaffold without GFs, and porous chitosan control.

Mechanical properties of the triphasic scaffolds. The highest tensile strength of the porous CHI scaffold was the lowest among the three groups, as illustrated in Fig. 3(C) (0.50 ± 0.03 MPa), while the triphasic scaffolds with and without GFs had much higher tensile strengths (1.63 ± 0.29 MPa *vs.* 1.61 ± 0.09 MPa; $P > 0.05$) than the porous CHI control ($P < 0.05$), demonstrating that while the addition of NPs had a minimal impact, the combination of electrospun nanofibers and CHI hydrogel enhanced the scaffolds' maximum tensile strength.

In vitro bioactivity of scaffolds

hPDLSC morphology, adhesion, and viability on the scaffolds. hPDLSCs were successfully isolated and characterized by their long spindle shape observed under a microscope and molecular phenotype of positive CD90, CD146, and negative CD45 expressions identified by flow cytometry (Fig. 4(A)). Fig. 4(B) shows that on the 3rd day, hPDLSCs were attached to the surface of all the scaffolds in an elongated, spindled, or fusiform morphology. In contrast to the PLA–PCL, hPDLSCs were better dispersed on the surfaces of PLA–PCL-NPs-BMP2 and PLA–PCL-NPs-rhCEMP1. With the elongation of culture time, PDLSCs on the surfaces of the three groups of scaffolds formed large areas of fusion on the 7th day. The live cells fluoresced green, whereas the dead cells fluoresced red under CLSM. As shown in Fig. 5(A), there were almost no dead cells in all the groups and there was no significant difference among the four groups ($P > 0.05$). The results suggested that the introduction of NPs-BMP2, NPs-rhCEMP1, and NPs-CTGF did not increase the cytotoxicity of triphasic scaffolds, and the combination of PLA–PCL and CHI had little effect on the cytotoxicity of scaffolds.

Then the seventh day was when all groups showed the maximum levels of cell proliferation, according to the CCK-8 results, and the blank control had significantly higher levels of

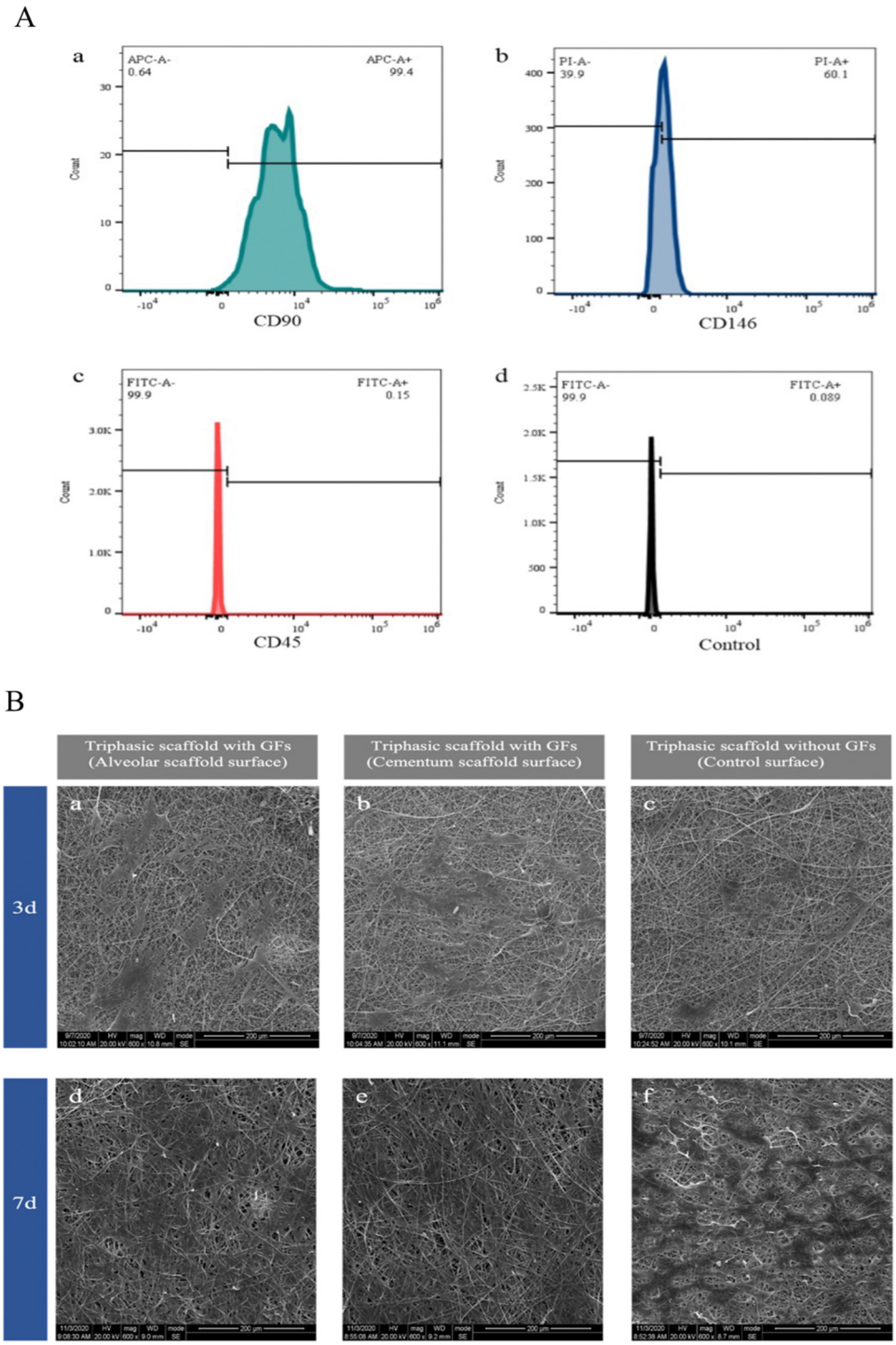

Fig. 4 (A) Molecular phenotype identification results of hPDLSCs by flow cytometry. (a) CD90, (b) CD146, (c) CD45, and (d) control group. (B) SEM images of PDLSCs adhering to the surface of the scaffolds on the 3rd and 7th day. (a) and (d) The surface of the alveolar bone layer of the triphasic scaffold with GFs. (b) and (e) The surface of the cementum layer of the triphasic scaffold with GFs. (c) and (f) The surface of the triphasic scaffold without GFs.

proliferation activity at each time point than the other three groups ($P < 0.05$). However, the triphasic scaffolds with GFs showed higher cell proliferation activity compared to the porous CHI control ($P < 0.05$ on the 1st, 4th, 7th, and 10th days) and the triphasic scaffolds without GFs ($P < 0.05$ on the 7th day), indicating that the loading of GFs promoted hPDLSCs proliferation and alleviated the moderate cytotoxicity of the scaffolds on cells (Fig. 5(B)).

hPDLSC osteogenesis/cementogenesis/fibrogenesis on the scaffolds. To further compare the influences of the alveolar

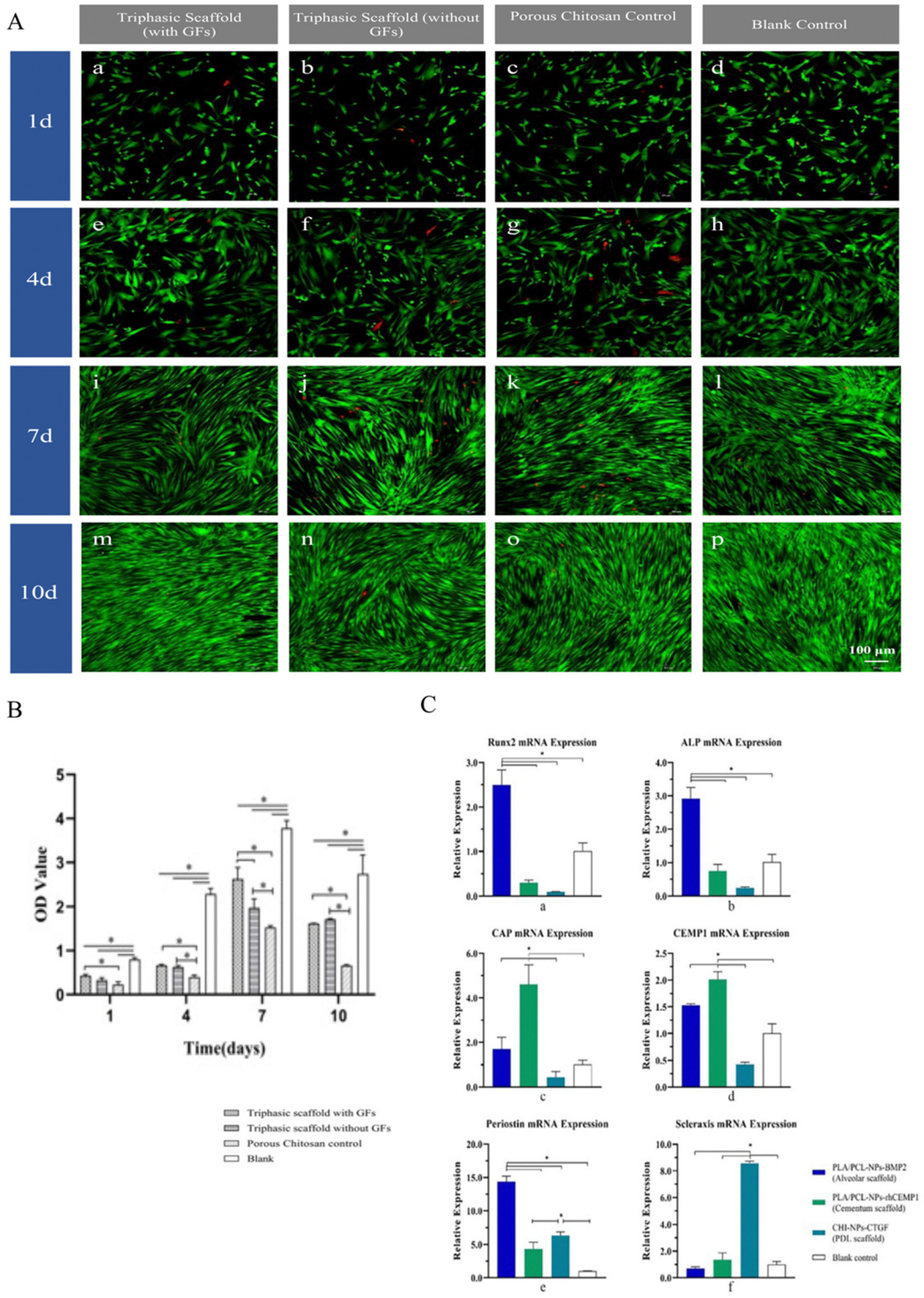

Fig. 5 (A) Laser confocal observation images of live and dead cells staining of hPDLSCs on the 1st, 4th, 7th, and 10th day of scaffolds leaching solution culture. (a), (e), (i) and (m) Triphasic scaffolds with GFs. (b), (f), (j) and (n) Triphasic scaffolds without GFs. (c), (g), (k) and (o) Porous chitosan control. (d), (h), (l) and (p) Blank control (green: live cells, red: dead cells). (100 μm). (B) CCK8 detection results. The proliferation activity of hPDLSCs on the 1st, 4th, 7th, and 10th day after incubating on the scaffolds. ("*" indicates statistical differences between groups). (C) Comparison of osteogenesis, cementogenesis, and periodontal ligament-related gene expression in hPDLSCs of triphasic scaffolds. (a) and (b) Osteogenesis-related genes. *RUNX2*, *ALP*. (c) and (d) Cementogenesis-related genes. *CAP*, *CEMP1*. (e) and (f) Periodontal ligament-related genes. *Periostin*, *Scleraxis*. ("*" indicates statistical differences between groups).

bone compartment, cementum compartment, and PDL compartment loaded with various GFs within the triphasic scaffolds on the committed differentiation potential of PDLSCs, hPDLSCs were cocultured with PLA–PCL-NPs-BMP2, PLA–PCL-NPs-rhCEMP1, and CHI-NPs-CTGF for 7 days, and the expressions of *Runx2*, *ALP*, *CAP*, *CEMP1*, *Periostin*, and *Scleraxis* were

measured, with the cells cultured alone serving as the blank control. For osteogenesis-related genes, the PLA–PCL-NPs-BMP2 group displayed the highest expression levels of *Runx2*, *ALP* ($P < 0.05$). For cementogenesis-related genes, the *CAP*, *CEMP1* expressions in the PLA–PCL-NPs-rhCEMP1 group ranked first ($P < 0.05$). For PDL-related genes, the CHI-NPs-CTGF group represented the most up-regulated tendency of the *Scleraxis* expression, while the expression of *Periostin* in PLA–PCL-NPs-BMP2 preceded the CHI-NPs-CTGF group ($P < 0.05$), both of which were higher than the PLA–PCL-NPs-rhCEMP1 ($P < 0.05$) (Fig. 5(C)).

Scaffolds guided repair in rat periodontal defects

Micro-CT measurement. Fig. 6(A) displays the 3D reconstructed topography of the defect areas in each group, and abundant newly formed mineralized bone deposition could be

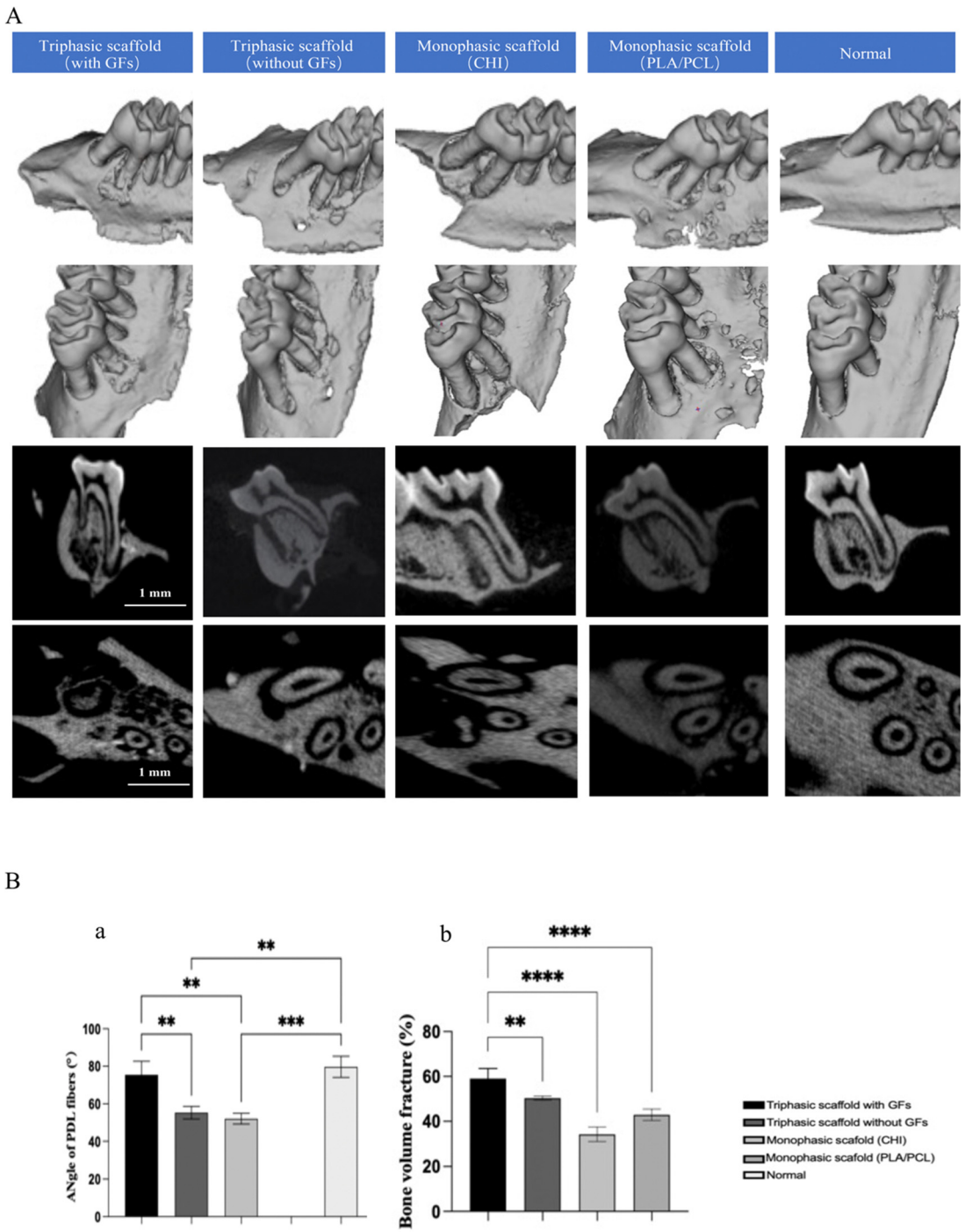

Fig. 6 (A) Repair of periodontal tissue defects in rats at 12 weeks after the operation. (B) Quantitative statistics of the repair of periodontal tissue defects in rats. (a) Comparison of the angle of PDL fibers of new periodontal ligament-like tissues. (b) Comparison of bone volume fractions of new alveolar bone-like tissue.

noted in the root apical region at the edge of the defect in the triphasic scaffold with GFs group, which was like the natural periodontal tissue. And the triphasic scaffold without GFs achieved relatively less regeneration of mineralized tissue. Meanwhile, in the two monophasic scaffold groups, only sporadic granular mineralized tissue could be observed scattering around the root surface. Quantitively, the BV/TV value in the triphasic scaffold group with GFs was higher than those of the other groups ($P < 0.05$) (Fig. 6(B)-b), implying that the biomimetic scaffolds with sustained delivery of different GFs were capable of recruiting hPLLSCs for subsequent long-lasting osteogenesis and mineralization in the orthotopic transplants.

Histological and immunohistochemical staining analyses. In the triphasic scaffold with the GF group, as seen in the H&E staining images displayed in Fig. 7(A)-a, the newly formed alveolar bone-like tissue was only seen in the root's apical region, whereas in the other groups, significant amounts of growing fibrous connective tissue were discovered to deposit around root surfaces. Observation illustrated that the collagen bundles were orderly arranged between the nascent alveolar bone-like tissue and root in the group of the triphasic scaffold with GFs, resembling the microstructure of natural PDL even though they were relatively sparse. The deposition of newly formed hyperchromatic cementum-like tissue around the root surface was also recognized. We further measured the angulations between the nascent collagen fiber bundles and the root surface using Image J software (Fig. 7(B)). The average angle between PDL-like tissue and root surface in the triphasic scaffold with the GFs group was perpendicular-like and very close to that of the physiological PDL in the normal control, which was much larger than those of the triphasic scaffold without GFs and monophasic CHI scaffold ($P < 0.05$) (Fig. 6(B)-a).

To further support periodontal regenerations, Masson trichrome staining was then performed (Fig. 7(A)-b). Blue dye was used to color the newly produced collagen strands, and it was noticeable that denser and larger amounts of collagen as well as mineralized bone tissue were presented in the triphasic scaffold with the GFs group. This result was in line with the H&E staining result that the triphasic scaffold with GFs had the best restoration effectiveness of all the groups. Furthermore, we conducted immunohistochemical staining to assess BMP2 expression (Fig. 7(A)-c). The staining in the triphasic scaffold with the GFs group indicated that this group has the best osteoinductive capacity and periodontal repair efficacy. Besides, BMP2 staining was significantly positive in both triphasic scaffold groups and the monophasic scaffold groups showed marginally positive staining.

Discussion

The periodontium's hierarchical architecture necessitates a highly coordinated regeneration process in which each component (cementum, PDL, and alveolar bone) reacts in accordance with distinct, occasionally overlapping spatiotemporal sequences.[31–33]

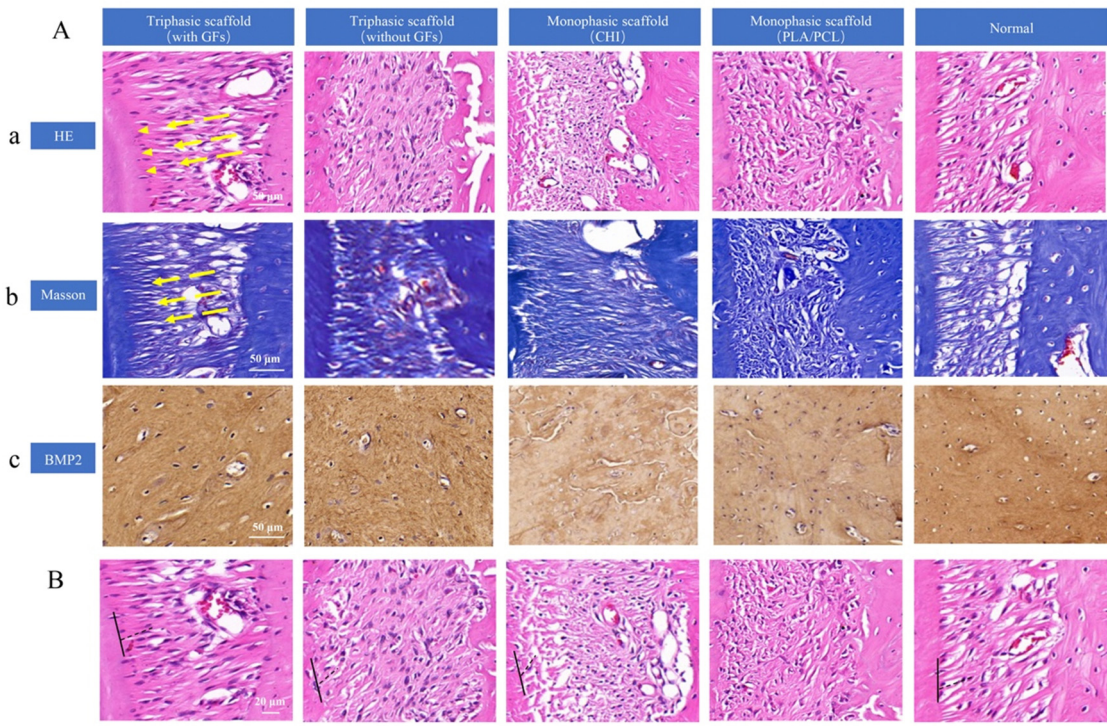

Fig. 7 (A) Repair of periodontal tissue defect in rats at 12 weeks after the operation. (a) Hematoxylin and eosin (H&E) staining images of each group. (50 μm, yellow arrows indicated the direction of the new periodontal ligament). (b) Masson staining images of each group. (50 μm). (c) The expressions of BMP2 in each group were assessed using immunohistochemical staining. (50 μm). (B) Comparison of angles of collagen fiber bundles in new periodontal ligament-like tissue (20 μm).

Since predictable periodontal regeneration hardly occurs during conventional therapy, the utilization of multiphasic constructs with either cells or biochemical cues, recapitulating the native anatomical topology, especially the submicron interfacial PDL geometry, has recently been advocated as the most promising strategy.[34] The current study suggests that putative alveolar bone, cementum-like structures, and a PDL-like tissue interface can be produced both *in vitro* and *in vivo* using PLA–PCL- and CHI-based triphasic scaffolds with three distinct microstructures and spatiotemporal delivery of BMP2, rhCEMP1, and CTGF in NPs. Each compartment's thickness complied with the periodontium's anatomical requirements.[14,19,35–39]

The diameters of electrospun nanofibers were in the range of 200–600 nm, while the pore sizes of CHI were in the range of 60–200 μm, which met the criteria of the natural ECM fibers to maintain sufficient mechanical strength and provide a favorable microenvironment for cell attachment, proliferation, and migration.[40] Also, the electrospun nanofibers on both sides of the triphasic scaffold were tightly stacked, simulating the lamellar structure of cementum and alveolar bone, according to the results of our SEM scanning.[35,41] The CHI hydrogel in the middle had a directionally arranged microporous channel structure, resulting in high porosity and interconnectivity, as well as low stiffness, which may be considered an important design criterion for tissue integration.[42] The structure provided the possibility to guide the directional regeneration of the PDL.

It is significant that the scaffold with a specified mechanical strength promotes selective cell repopulation and wound stability, prevents undesirable tissue invasion, and serves as space maintenance to promote the development of functional tissues that are dimensionally stable over time.[34,43,44] The PCL adopted is extensively used in the regeneration of mineralized tissues owing to superior biocompatibility, water degradability, toughness, and mechanical strength.[45] However, the low surface energy of PCL impedes cell adhesion and tissue integration, and the slow degradation rate was also unfavorable to further ingrowth and maturation of regenerated tissues.[46,47] In contrast, PLA has higher brittleness but good biocompatibility.[22,23] As a naturally degradable polysaccharide in ECM, CHI possesses excellent hydrophily, fluidity, adhesiveness, and antibacterial properties and is widely applied in tissue regeneration, wound healing, and other fields.[48] Moreover, CHI has a morphological structure analogous to the extracellular matrix (ECM), and it acts as a biological glue to bond materials such as electrospun nanofibers.[49] With the current study's freeze-dried CHI hydrogel, a specific porosity structure allowed for huge transportation to help with biological delivery, cell infiltration, and tissue regeneration.[50–52]

BMP2 is a member of the transforming growth factor-β superfamily, which promotes the differentiation of various stem cells such as dental follicle cells and hPDLSCs into osteoblasts, and this can accelerate the formation of alveolar bone tissue.[53–55] CEMP1 isolated from cementum, promotes the differentiation of hPDLSCs into cementoblasts while inhibiting its osteogenic differentiation.[56–58] CTGF plays an important role in maintaining and repairing periodontal ligament integrity by promoting fibrogenic differentiation and upregulating the expression of collagen type I and III and periostin.[19,59,60] Due to the short half-life and easy inactivation of bioactive components *in vitro*, local delivery and sustained release of them cannot be achieved if they are directly combined with a scaffold by immersion, covalent binding, or other methods.[61–64] Therefore, it is crucial to develop more advanced methods to distribute these bioactive compounds in a controlled and sustained manner while also minimizing their negative effects. Using NPs stabilized by BSA and CHI, we loaded BMP2, rhCEMP, and CTGF into the alveolar bone, cement, and PDL compartments, respectively, based on the procedures outlined in earlier investigations.[26] The EE of NPs was rather high, and their sustained release could be detected until the 30th day, which was consistent with the previous study.[26] Interestingly, we found that CTGF, which promotes ligament differentiation, was released in a more robust manner than BMP2 and rhCEMP1 during the first three days, which is speculated to be better for the repair and regeneration of periodontal tissue.

On the 7th day, the number and fusion area of hPDLSCs on the alveolar and cementum surfaces of triphasic scaffolds with GFs were significantly larger than the other groups, proving the capacity of cell adhesion and alignment guidance for both the alveolar bone and cementum compartments. Indicated time points showed that the triphasic scaffold group with GFs had higher cell proliferation activity than the other groups, demonstrating that the GFs loading increased hPDLSCs proliferation and reduced the mild cytotoxicity of the scaffolds on cells in a time-dependent manner. We hypothesized that this pattern might be related to the cumulative concentrations of BMP2, rhCEMP1, and CTGF in a certain period, which promoted cell proliferation and differentiation.[65–67] The studies of Cattaneo,[68] Jhala,[69] and Mcbeath[70] all showed that the cells with flattened morphology tended to differentiate into osteoblasts and cementoblasts rather than fibroblasts. Results showed that both PLA–PCL-NPs-BMP2 and PLA–PCL-NPs-rhCEMP1 tended to induce the osteogenic differentiation of hPDLSCs. Unexpectedly, we discovered that the expression of *Periostin* in the CHI-NPs-CTGF was lower than that in the PLA–PCL-NPs-BMP2. The reason might be that *Periostin* expression was not specifically confined to the PDL, it is also highly expressed in the bone tissue and could be effectively promoted by BMP2 treatment.[66,71,72]

Here, we have successfully generated a rat model of surgically induced periodontal lesions in the maxillary first molar and assessed the *in vivo* effectiveness of the scaffolds. Collagen bundles were oriented between the newly created alveolar bone-like tissue and root in the triphasic scaffold with the GFs group. In addition, intricate integrations between collagen bundles and tissue that resembled the cementum and the PDL–cementum interface were created at the same time. The fibrous connective tissue in the other groups, however, was disordered and lacked trim configurations, and no collagen bundles had developed. The anchoring of the newly generated fiber bundles into a cementum-like mineralized layer on the root surface was

further confirmed by Masson and IHC staining. Our research has shown that triphasic scaffolds with biomimetic geometries can effectively support the regrowth, arranging, and structuring of physiological periodontal tissues.

Despite all these encouraging outcomes for this scaffold *in vitro* and *in vivo*, there are still several constraints. The recent research primarily showed that both ends of fibrous PDL bundles were anchored into the cementum and alveolar bone, which act as connectors between mineralized tissues, although the underlying mechanisms were still not fully understood. However, the *in vivo* models were still limited to larger animals. This hampered the direct translation into preclinical and clinical treatment. Consequently, further research will need to be done in the future to confirm the translational use of this scaffold.

Conclusions

In this study, we successfully fabricated a biomimetic GF-loaded triphasic scaffold with regional-specific geometry, which highly simulated the native architecture of alveolar bone, PDL, and cementum. *In vitro*, the scaffolds were validated to possess favorable mechanical properties, excellent biocompatibility, and low cytotoxicity. Each compartment of the construct with indicated GFs could promote the expression of osteogenesis-related, periodontal ligament-related, and cementogenesis-related genes in PDLSCs. *In vivo*, the biomimetic scaffolds loaded with GFs were also demonstrated to repair the periodontal defects in rats by promoting the formation of the physiological periodontium. Overall, despite some drawbacks, our work provides a novel approach for recapitulating the physiologic organization and function of the periodontal tissue with multiphasic scaffolds.

Author contributions

Weihan Hua: conceptualization, methodology, data curation, formal analysis, writing – original draft, and validation. Jie Xiang: methodology, validation, formal analysis, and software. Yeke Wu: methodology, data curation, funding acquisition, and validation. Wei Yang: conceptualization, project administration, and writing – review & editing. Lixing Zhao: conceptualization, funding acquisition, project administration, and writing – review & editing.

Conflicts of interest

There are no conflicts to declare.

Acknowledgements

This research was supported by grants from the National Nature Science Foundation of China (no. 81973684, 31271052, 31670992) and the Nature Science Foundation of Sichuan (no. 2574).

References

1 W. Guo, L. Chen, K. Gong, B. Ding, Y. Duan and Y. Jin, *Tissue Eng., Part A*, 2012, **18**, 459–470.
2 S. Yao, F. Pan, V. Prpic and G. E. Wise, *J. Dent. Res.*, 2008, **87**, 767–771.
3 P. M. Bartold, S. Shi and S. Gronthos, *Periodontol 2000*, 2006, **40**, 164–172.
4 S. Sowmya, K. P. Chennazhi, H. Arzate, P. Jayachandran, S. V. Nair and R. Jayakumar, *Tissue Eng., Part C*, 2015, **21**, 1044–1058.
5 C. A. Ramseier, A. Anerud, M. Dulac, M. Lulic, M. P. Cullinan, G. J. Seymour, M. J. Faddy, W. Bürgin, M. Schätzle and N. P. Lang, *J. Clin. Periodontol.*, 2017, **44**, 1182–1191.
6 J. Pyo, M. Lee, M. Ock and J. Lee, *Int. J. Environ. Res. Public Health*, 2020, **17**, 4895.
7 D. R. Meusel, J. C. Ramacciato, R. H. Motta, R. B. Brito Júnior and F. M. Flório, *J. Oral Sci.*, 2015, **57**, 87–94.
8 A. Caygur, M. R. Albaba, A. Berberoglu and H. G. Yilmaz, *J. Int. Med. Res.*, 2017, **45**, 1168–1174.
9 D. E. Deas, A. J. Moritz, R. S. Sagun, Jr., S. F. Gruwell and C. A. Powell, *Periodontol 2000*, 2016, **71**, 128–139.
10 I. Darby, *Aust. Dent. J.*, 2011, **56**(Suppl 1), 107–118.
11 C. Vaquette, S. Saifzadeh, A. Farag, D. W. Hutmacher and S. Ivanovski, *J. Dent. Res.*, 2019, **98**, 673–681.
12 P. F. Costa, C. Vaquette, Q. Zhang, R. L. Reis, S. Ivanovski and D. W. Hutmacher, *J. Clin. Periodontol.*, 2014, **41**, 283–294.
13 C. Vaquette, W. Fan, Y. Xiao, S. Hamlet, D. W. Hutmacher and S. Ivanovski, *Biomaterials*, 2012, **33**, 5560–5573.
14 C. H. Park, H. F. Rios, Q. Jin, M. E. Bland, C. L. Flanagan, S. J. Hollister and W. V. Giannobile, *Biomaterials*, 2010, **31**, 5945–5952.
15 C. H. Park, H. F. Rios, Q. Jin, J. V. Sugai, M. Padial-Molina, A. D. Taut, C. L. Flanagan, S. J. Hollister and W. V. Giannobile, *Biomaterials*, 2012, **33**, 137–145.
16 E. C. Carlo Reis, A. P. Borges, M. V. Araújo, V. C. Mendes, L. Guan and J. E. Davies, *Biomaterials*, 2011, **32**, 9244–9253.
17 W. Jiang, L. Li, D. Zhang, S. Huang, Z. Jing, Y. Wu, Z. Zhao, L. Zhao and S. Zhou, *Acta Biomater.*, 2015, **25**, 240–252.
18 C. H. Park, J. H. Oh, H. M. Jung, Y. Choi, S. U. Rahman, S. Kim, T. I. Kim, H. I. Shin, Y. S. Lee, F. H. Yu, J. H. Baek, H. M. Ryoo and K. M. Woo, *Acta Biomater.*, 2017, **61**, 134–143.
19 C. H. Lee, J. Hajibandeh, T. Suzuki, A. Fan, P. Shang and J. J. Mao, *Tissue Eng., Part A*, 2014, **20**, 1342–1351.
20 S. Sowmya, U. Mony, P. Jayachandran, S. Reshma, R. A. Kumar, H. Arzate, S. V. Nair and R. Jayakumar, *Adv. Healthcare Mater.*, 2017, **6**, 10.
21 M. Wu, J. Wang, Y. Zhang, H. Liu and F. Dong, *Med. Sci. Monit.*, 2018, **24**, 1112–1123.
22 F. Diomede, A. Gugliandolo, P. Cardelli, I. Merciaro, V. Ettorre, T. Traini, R. Bedini, D. Scionti, A. Bramanti, A. Nanci, S. Caputi, A. Fontana, E. Mazzon and O. Trubiani, *Stem Cell Res. Ther.*, 2018, **9**, 104.

23 T. Xu, Q. Yao, J. M. Miszuk, H. J. Sanyour, Z. Hong, H. Sun and H. Fong, *Colloids Surf., B*, 2018, **171**, 31–39.
24 M. Sun and S. Downes, *J. Mater. Sci.: Mater. Med.*, 2009, **20**, 1181–1192.
25 M. Sun, P. J. Kingham, A. J. Reid, S. J. Armstrong, G. Terenghi and S. Downes, *J. Biomed. Mater. Res., Part A*, 2010, **93**, 1470–1481.
26 L. Li, G. Zhou, Y. Wang, G. Yang, S. Ding and S. Zhou, *Biomaterials*, 2015, **37**, 218–229.
27 P. Divakar, K. Yin and U. G. K. Wegst, *J. Mech. Behav. Biomed. Mater.*, 2019, **90**, 350–364.
28 G. Huang, F. Li, X. Zhao, Y. Ma, Y. Li, M. Lin, G. Jin, T. J. Lu, G. M. Genin and F. Xu, *Chem. Rev.*, 2017, **117**, 12764–12850.
29 Z. M. Goudarzi, T. Behzad, L. Ghasemi-Mobarakeh and M. Kharaziha, *Polymer*, 2021, **213**, 123313.
30 M. Zhang, Y. Ma, R. Li, J. Zeng, Z. Li, Y. Tang and D. Sun, *J. Biomater. Sci., Polym. Ed.*, 2017, **28**, 2205–2219.
31 Y. Yang, F. M. Rossi and E. E. Putnins, *Biomaterials*, 2010, **31**, 8574–8582.
32 R. Raju, M. Oshima, M. Inoue, T. Morita, Y. Huijiao, A. Waskitho, O. Baba, M. Inoue and Y. Matsuka, *Sci. Rep.*, 2020, **10**, 1656.
33 S. Ivanovski, *Aust. Dent. J.*, 2009, **54**(Suppl 1), S118–S128.
34 C. Vaquette, S. P. Pilipchuk, P. M. Bartold, D. W. Hutmacher, W. V. Giannobile and S. Ivanovski, *Adv. Healthcare Mater.*, 2018, **7**, e1800457.
35 S. P. Ho, M. P. Kurylo, K. Grandfield, J. Hurng, R. P. Herber, M. I. Ryder, V. Altoe, S. Aloni, J. Q. Feng, S. Webb, G. W. Marshall, D. Curtis, J. C. Andrews and P. Pianetta, *Bone*, 2013, **57**, 455–467.
36 A. Nanci and D. D. Bosshardt, *Periodontol 2000*, 2006, **40**, 11–28.
37 M. G. Kim and C. H. Park, *Molecules*, 2020, **25**, 4802.
38 G. Rasperini, S. P. Pilipchuk, C. L. Flanagan, C. H. Park, G. Pagni, S. J. Hollister and W. V. Giannobile, *J. Dent. Res.*, 2015, **94**, 153s–157s.
39 S. P. Pilipchuk, A. Monje, Y. Jiao, J. Hao, L. Kruger, C. L. Flanagan, S. J. Hollister and W. V. Giannobile, *Adv. Healthcare Mater.*, 2016, **5**, 676–687.
40 W. Zhang, Z. He, Y. Han, Q. Jiang, C. Zhan, K. Zhang, Z. Li and R. Zhang, *Composites, Part A*, 2020, **137**, 106009.
41 T. van den Bos and W. Beertsen, *J. Periodontal Res.*, 1999, **34**, 1–6.
42 C. H. Park, K. H. Kim, H. F. Rios, Y. M. Lee, W. V. Giannobile and Y. J. Seol, *J. Dent. Res.*, 2014, **93**, 1304–1312.
43 J. Gottlow, T. Karring and S. Nyman, *J. Periodontol.*, 1990, **61**, 680–685.
44 J. Gottlow, S. Nyman, J. Lindhe, T. Karring and J. Wennström, *J. Clin. Periodontol.*, 1986, **13**, 604–616.
45 T. K. Teh, S. L. Toh and J. C. Goh, *Tissue Eng., Part A*, 2013, **19**, 1360–1372.
46 R. Dwivedi, S. Kumar, R. Pandey, A. Mahajan, D. Nandana, D. S. Katti and D. Mehrotra, *J. Oral Biol. Craniofacial Res.*, 2020, **10**, 381–388.
47 W. Wang, G. Caetano, W. S. Ambler, J. J. Blaker, M. A. Frade, P. Mandal, C. Diver and P. Bártolo, *Materials*, 2016, **9**, 992.
48 A. Francesko and T. Tzanov, *Adv. Biochem. Eng./Biotechnol.*, 2011, **125**, 1–27.
49 I. Y. Kim, S. J. Seo, H. S. Moon, M. K. Yoo, I. Y. Park, B. C. Kim and C. S. Cho, *Biotechnol. Adv.*, 2008, **26**, 1–21.
50 Y. Liao, H. Li, R. Shu, H. Chen, L. Zhao, Z. Song and W. Zhou, *Front. Cell. Infect. Microbiol.*, 2020, **10**, 180.
51 E. M. Varoni, S. Vijayakumar, E. Canciani, A. Cochis, L. De Nardo, G. Lodi, L. Rimondini and M. Cerruti, *J. Dent. Res.*, 2018, **97**, 303–311.
52 D. G. Miranda, S. M. Malmonge, D. M. Campos, N. G. Attik, B. Grosgogeat and K. Gritsch, *J. Biomed. Mater. Res., Part B*, 2016, **104**, 1691–1702.
53 M. Ou, Y. Zhao, F. Zhang and X. Huang, *Connect. Tissue Res.*, 2015, **56**, 204–211.
54 S. Y. Hyun, J. H. Lee, K. J. Kang and Y. J. Jang, *Mol. Cells*, 2017, **40**, 550–557.
55 J. Tan, M. Zhang, Z. Hai, C. Wu, J. Lin, W. Kuang, H. Tang, Y. Huang, X. Chen and G. Liang, *ACS Nano*, 2019, **13**, 5616–5622.
56 M. Komaki, K. Iwasaki, H. Arzate, A. S. Narayanan, Y. Izumi and I. Morita, *J. Cell. Physiol.*, 2012, **227**, 649–657.
57 H. Arzate, M. Zeichner-David and G. Mercado-Celis, *Periodontol 2000*, 2015, **67**, 211–233.
58 L. Hoz, E. Romo, M. Zeichner-David, M. Sanz, J. Nuñez, L. Gaitán, G. Mercado and H. Arzate, *Cell Biol. Int.*, 2012, **36**, 129–136.
59 A. Yuda, H. Maeda, S. Fujii, S. Monnouchi, N. Yamamoto, N. Wada, K. Koori, A. Tomokiyo, S. Hamano, D. Hasegawa and A. Akamine, *J. Cell. Physiol.*, 2015, **230**, 150–159.
60 J. W. Choi, C. Arai, M. Ishikawa, S. Shimoda and Y. Nakamura, *J. Periodontal Res.*, 2011, **46**, 513–521.
61 C. Uggen, J. Dines, M. McGarry, D. Grande, T. Lee and O. Limpisvasti, *Arthroscopy*, 2010, **26**, 1456–1462.
62 T. Tokunaga, J. Ide, H. Arimura, T. Nakamura, Y. Uehara, H. Sakamoto and H. Mizuta, *Arthroscopy*, 2015, **31**, 1482–1491.
63 M. S. Lee, T. Ahmad, J. Lee, H. K. Awada, Y. Wang, K. Kim, H. Shin and H. S. Yang, *Biomaterials*, 2017, **124**, 65–77.
64 Y. C. Jiang, X. F. Wang, Y. Y. Xu, Y. H. Qiao, X. Guo, D. F. Wang, Q. Li and L. S. Turng, *Biomacromolecules*, 2018, **19**, 3747–3753.
65 G. N. King and F. J. Hughes, *J. Clin. Periodontol.*, 2001, **28**, 465–475.
66 A. Skodje, S. B. Idris, Y. Sun, S. Bartaula, K. Mustafa, A. Finne-Wistrand, U. M. Wikesjö and K. N. Leknes, *J. Biomed. Mater. Res., Part A*, 2015, **103**, 1991–1998.
67 N. H. Heng, J. Zahlten, V. Cordes, M. M. Ong, B. T. Goh, P. D. N'Guessan and N. Pischon, *J. Periodontol.*, 2015, **86**, 569–577.
68 V. Cattaneo, C. Rota, M. Silvestri, C. Piacentini, A. Forlino, A. Gallanti, G. Rasperini and G. Cetta, *J. Periodontal Res.*, 2003, **38**, 568–574.
69 D. Jhala, H. Rather and R. Vasita, *Biomater. Sci.*, 2016, **4**, 1584–1595.
70 R. McBeath, D. M. Pirone, C. M. Nelson, K. Bhadriraju and C. S. Chen, *Dev. Cell*, 2004, **6**, 483–495.
71 J. Du and M. Li, *Adv. Exp. Med. Biol.*, 2019, **1132**, 63–72.
72 K. Inai, R. A. Norris, S. Hoffman, R. R. Markwald and Y. Sugi, *Dev. Biol.*, 2008, **315**, 383–396.